

Dynamics of flags over wide ranges of mass and bending stiffness

Silas Alben*

Department of Mathematics, University of Michigan, Ann Arbor, Michigan 48109, USA



(Received 28 June 2021; accepted 22 December 2021; published 18 January 2022)

There have been many studies of the instability of a flexible plate or flag to flapping motions, and of large-amplitude flapping. Here we use inviscid simulations and a linearized model to more generally study how key quantities—mode number (or wave number), frequency, and amplitude—depend on the two dimensionless parameters: flag mass and bending stiffness. In the limit of small flag mass, flags perform traveling wave motions that move at nearly the speed of the oncoming flow. The flag mode number scales as the $-1/4$ power of bending stiffness. The flapping frequency has the same scaling, with an additional slight increase with flag mass in the small-mass regime. The flapping amplitude scales approximately as flag mass to the $1/2$ power. For large flag mass, the dominant mode number is low (0 or 1), the flapping frequency tends to zero, and the amplitude saturates in the neighborhood of its upper limit (the flag length). In a linearized model, the fastest growing modes have somewhat different power law scalings for wave number and frequency. We discuss how the numerical scalings are consistent with a weakly nonlinear model.

DOI: [10.1103/PhysRevFluids.7.013903](https://doi.org/10.1103/PhysRevFluids.7.013903)

I. INTRODUCTION

There have been many experimental and theoretical studies of the flutter of flexible plates or flags in recent years [1–18], following earlier work in the field of aeroelasticity [19–21]. Recent extensions include multiple-flag or flag-boundary interactions [22–27], three-dimensional effects [11,28–30], inverted flags [31–33], and applications to energy harvesting [34–38] and heat transfer [39–44]. Many of these studies addressed the stability problem: determining the region in parameter space where a flag in a uniform flow becomes unstable to transverse oscillations. Many studies have also characterized the flag dynamics that occur after the instability grows to large-amplitude flapping, including the transitions from periodic to chaotic motions [12,45,46]. Well-resolved viscous simulations can be expensive at high Reynolds number (Re), making it challenging to sweep large regions of parameter space. Inviscid fluid-structure interaction simulations are generally much less expensive than high-Re viscous solvers because quantities only need to be tracked on solid boundaries and vortex sheet wakes. The computational costs are greatly reduced when the vortex sheet wakes are approximated in the far field. Therefore, inviscid models are suitable for computing solutions throughout the regions of parameter space where their assumptions are physically valid. Some of the challenges of inviscid models compared to viscous solvers include less theoretical and computational development for fluid-structure interaction, a more limited range of physical validity, and less robustness in some cases. Chen *et al.* [46] developed a vortex panel model to study the inviscid dynamics of a flapping flag at a particular ratio of flag-to-fluid mass, and over a range of dimensionless flow velocity starting at the stability threshold and increasing by a factor of almost 20. As velocity is increased above the stability threshold, the flag flaps in a range of periodic states

*alben@umich.edu

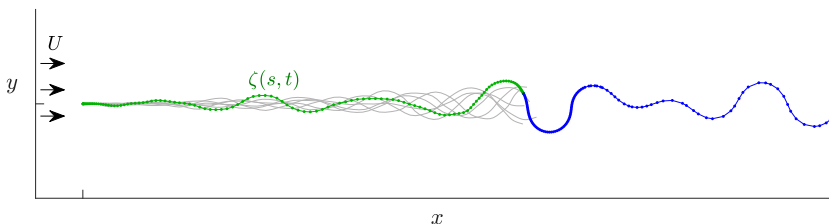


FIG. 1. Example of flag snapshots (gray and green lines) and vortex sheet wake (blue line) for $R_1 = 10^{-2.5}$ and $R_2 = 10^{-5.05}$. The green and blue lines are the flag and wake positions at $t = 9.5$. The gray lines are the flag positions at six equally spaced times from $t = 5.375$ to 9.0 in increments of 0.725 .

with a single dominant frequency, and then at a certain velocity, jumps to a mode with a much higher flapping frequency. Then a sequence of quasiperiodic bifurcations leads to a range of chaotic states, followed by a range of periodic states with a higher bending mode, and a sequence of bifurcations leading to chaotic flapping. In all, five ranges of periodic states were observed, one with up-down asymmetry, interspersed with period-doubling and quasiperiodic bifurcations, and three ranges of chaotic states. During this sequence of states, the flapping amplitude first increases by about a factor of 2, then decreases by about the same factor. The frequency mostly increases, by about a factor of 2.

In the present work, we use a similar inviscid model [45,47] to probe the flag dynamics, varying dimensionless bending stiffness (equivalent to varying dimensionless velocity) and varying the flag-to-fluid mass ratio. Rather than focusing on a single mass ratio, we study the flag dynamics over 6.5 orders of magnitude of the mass ratio. At intermediate mass ratios, we observe periodic and chaotic states similar to those in [46]. We do not study the sequences of states in detail here; our focus instead is on determining to what extent basic dynamical quantities—amplitude, frequency, and flapping mode number—can be approximated by simple scaling-law formulas. Most studies have focused on flapping in low bending modes (i.e., with few deflection peaks), which are easier to study experimentally and computationally. Large fabric flags may have much smaller dimensionless bending rigidities than those studied in most previous experiments, and in field observations they may exhibit traveling waves of deflection with fine wrinkled features corresponding to very high bending modes [48–50]. Of particular interest here is the dynamics in the limit of very light and flexible flags, where we find that stable high-mode-number, high-frequency, and small-amplitude (but nonlinear) bending modes can occur.

II. MODEL

We consider a thin plate or flag clamped at its leading edge in an oncoming flow (see Fig. 1). A sequence of flag snapshots are shown in gray, and in green at the latest time, together with the vortex sheet wake in blue, emanating from the flag’s trailing edge. Because the flow is inviscid, the vorticity remains confined to vortex sheets along the flag and the wake, which correspond to attached and separated viscous boundary layers in the limit of zero thickness. A uniform horizontal flow with velocity $U\mathbf{e}_x$ has been applied at infinity upstream, and the flag, wake, and flow evolve under the following system of equations which we first summarize: Euler’s equations of fluid momentum balance; the no-penetration condition on the flag; a mechanical force balance between flag bending stiffness, inertia, and fluid pressure; Kelvin’s circulation theorem; the Birkhoff-Rott equation for free vortex sheet dynamics; and the Kutta condition governing vorticity production at the flag’s trailing edge. We will present the most important equations here and refer to previous work [45,47,51,52] for the remainder and additional background information. In the following, we nondimensionalize lengths by half the flag length, L , velocities by the imposed flow speed U , and densities by the fluid density ρ_f .

The position of the (inextensible) flag is described as $\zeta(s, t) = x(s, t) + iy(s, t)$, $-1 \leq s \leq 1$, a curvilinear segment of length 2 in the complex plane, parametrized by arc length s and time t . The flow is an inviscid potential flow, so at each instant it may be computed in terms of quantities on the flag (the boundary of the flow domain) and on the vortex sheet wake. The vortex sheet has two parts: a “bound” part, coincident with the flag itself, for $-1 \leq s \leq 1$, and a “free” part, for $1 < s < 1 + L_w$, representing a vortex wake of length L_w that emanates from the flag’s trailing edge at $s = 1$. On both parts, the vortex sheet’s strength is denoted $\gamma(s, t)$ and its position is denoted $\zeta(s, t)$ (the same as the flag’s position for $-1 \leq s \leq 1$). The bound vortex sheet strength evolves to satisfy the no-penetration condition on the flag (but not the no-slip condition, since the flow is inviscid),

$$\text{Im}[e^{-i\theta(s,t)} \partial_t \zeta(s, t)] = \text{Im} \left\{ e^{-i\theta(s,t)} \left[1 + \int_{-1}^{L_w+1} \gamma(s', t) \overline{K(s, s', t)} ds' \right] \right\}, \quad -1 \leq s \leq 1. \quad (1)$$

This condition sets the component of the flag’s velocity normal to the flag [the left-hand side of (1)] equal to the same component of the flow velocity [the right-hand side of (1)]. Here, $\theta(s, t)$ is the tangent angle of the flag. The unity term inside the parentheses on the right-hand side is the uniform background flow and $K(s, s', t)$ is the complex flow velocity at $\zeta(s, t)$ due to a point vortex of strength unity located at $\zeta(s', t)$. The special integral symbol in (1) denotes a principal-value integral, due to the $\sim 1/(s - s')$ singularity in $K(s, s', t)$. The kernel is given by

$$K(s, s', t) = \frac{1}{2\pi i} \frac{1}{\zeta(s, t) - \zeta(s', t)}, \quad -1 \leq s, s' \leq 1. \quad (2)$$

We use a regularized version of the kernel on the free vortex sheet ($s' > 1$), which allows for smooth vortex sheet dynamics [53]:

$$K(s, s', t) = \frac{1}{2\pi i} \frac{\overline{\zeta(s, t) - \zeta(s', t)}}{|\zeta(s, t) - \zeta(s', t)|^2 + \delta(s', t)^2}, \quad -1 \leq s \leq 1, \quad s' > 1, \quad (3)$$

where the overbar gives the complex conjugate, and we set

$$\delta(s', t) = \delta_0 [1 - e^{-|\zeta(1, t) - \zeta(s', t)|^2 / 4\delta_0^2}], \quad (4)$$

with $\delta_0 = 0.2$. This regularization tapers to zero at the trailing edge, $s' = 1$, so $K(s, s', t)$ is continuous there. The tapered regularization allows for smooth vortex sheet dynamics away from the trailing edge, while decreasing the effect of regularization on the generation of vorticity at the trailing edge [54]. At the trailing edge, the vortex sheet is advected away from the flag by the uniform background flow, so it remains in the less regularized region near $s' = 1$ for a time that is too short to allow chaotic dynamics to develop. In [47,54], we found that the body deflection and/or wake vorticity vary by a few percent or less when δ_0 is 0.2 or smaller in the tapered distribution (4).

The vortex sheet strength $\gamma(s, t)$ is coupled to the pressure jump $[p](s, t)$ across the flag using a version of the unsteady Bernoulli equation [55,56],

$$\partial_t \gamma(s, t) + \partial_s \{ [\mu(s, t) - \tau(s, t)] \gamma(s, t) \} = \partial_s [p](s, t), \quad -1 \leq s \leq 1. \quad (5)$$

Here, $\mu(s, t)$ is the component of the flow velocity tangent to the flag,

$$\mu(s, t) = \text{Re} \left\{ e^{-i\theta(s,t)} \left[1 + \int_{-1}^{1+L_w} \gamma(s', t) \overline{K(s, s', t)} ds' \right] \right\}, \quad (6)$$

and $\tau(s, t)$ is the flag’s velocity component tangent to itself,

$$\tau(s, t) = \text{Re}[e^{-i\theta(s,t)} \partial_t \zeta(s, t)]. \quad (7)$$

The unsteady Euler-Bernoulli beam equation couples the pressure loading to flag inertia and bending stiffness (spatially uniform),

$$R_1 \partial_{tt} \zeta + R_2 \partial_s [\partial_s \kappa(s, t) i e^{i\theta(s,t)}] - \partial_s [T(s, t) e^{i\theta(s,t)}] = -[p] i e^{i\theta(s,t)}. \quad (8)$$

Here, R_1 and R_2 are the dimensionless material parameters for the flag,

$$R_1 = \frac{\rho_s h}{\rho_f L}, \quad R_2 = \frac{B}{\rho_f U^2 L^3 W}, \quad (9)$$

where ρ_s is the mass per unit volume of the flag and h is its thickness. We assume that h/L is small, but ρ_s/ρ_f may be large, so R_1 may assume any non-negative value. As stated previously, ρ_f is the mass per unit volume of the fluid and L is half the flag length. B is the flag bending stiffness, U is the uniform background flow speed, and W is the out-of-plane width of the flag. The flow is assumed to be two dimensional (2D), so it is uniform in the out-of-plane direction. In (8), $\kappa = \partial_s \theta$ is the beam's curvature and $T(s, t)$ is the tension in the flag, arising from its inextensibility. T is eliminated in terms of κ by integrating the tangential component of (8) from the free end of the flag ($s = 1$) where $T = 0$ (and $\kappa = \partial_s \kappa = 0$). The normal component of (8) is then used to relate $[p]$ to the flag shape and motion given by ζ and κ , with ‘‘clamp’’ boundary conditions described below in Eq. (10). Further details are given in a previous work [47]. We also refer the reader to this work for information on how the vorticity in the free vortex sheet is generated at the trailing edge using the Kutta condition, and advected in the flow using the Birkhoff-Rott equation.

We evolve the flag and flow using the equations just presented, as an initial-boundary-value problem, with the flag starting in the horizontal state with uniform flow velocity $U \mathbf{e}_x$ at $t = 0$. The flag's position and tangent angle at its upstream edge ($s = -1$) are given a slight perturbation from the horizontal state that is significant only near $t = 0$:

$$\begin{aligned} \zeta(-1, t) &= i0.02(t/0.2)^3 e^{-(t/0.2)^3}, \\ \theta(-1, t) &= 0.02(t/0.2)^3 e^{-(t/0.2)^3}, \quad t \geq 0. \end{aligned} \quad (10)$$

We then compute the flag and flow for $t > 0$. For some (R_1, R_2) values, as t exceeds 1 the flag deflection decays exponentially with time, and tends to the flat, horizontal state—a stable equilibrium. For other (R_1, R_2) values, the flag deflection grows rapidly (sometimes exponentially) with time, in which case the flat state is unstable.

In the following section, we characterize the large-amplitude dynamics of the flag (mode number, dominant frequency, and amplitude) and how they depend on the parameters. We will see that in some cases, the steady-state dynamics are periodic or chaotic with a deflection amplitude that is very small compared to the flag length—much smaller than that in Fig. 1 in some cases. Although the deflection amplitude is small, the initial instability has reached saturation due to nonlinear effects.

III. SIMULATION RESULTS

In Fig. 2, we show typical flag snapshots arranged approximately by their locations in (R_1, R_2) space. The horizontal midpoints of the flags are located above the corresponding R_1 (mass) values, labeled on the horizontal axis at the bottom, and ranging from $10^{-4.5}$ to 10^2 . The smaller values correspond to flags with very small mass density, which could be less than that of the surrounding fluid, depending on the flag thickness. Although the flag thickness is approximated as zero in the flow plane, it is assumed to be small but nonzero in the physical parameters, corresponding to nonzero mass density and bending stiffness. Above each R_1 value, one to four sets of flag snapshots are stacked in a vertical column, and the corresponding values of R_2 (bending stiffness) are marked by the positions of the colored dots below the column of snapshots, relative to the R_2 axis on the left side. The dots lie on a gray line that marks the range of R_2 values simulated at that R_1 , generally covering two to three orders of magnitude of R_2 decreasing from the stability boundary, but a smaller range at the smallest R_1 value. In each column, the uppermost dot and uppermost set of snapshots are close to the stability boundary, and periodic flapping generally occurs there. Lower sets of snapshots correspond to periodic flapping in higher bending modes ($10^{-1.5} \leq R_1 \leq 10^{-0.5}$) or, more commonly, chaotic flapping that can be up-down asymmetric in some cases (e.g., lower sets of snapshots at $R_1 = 10^0$ and $10^{0.5}$).

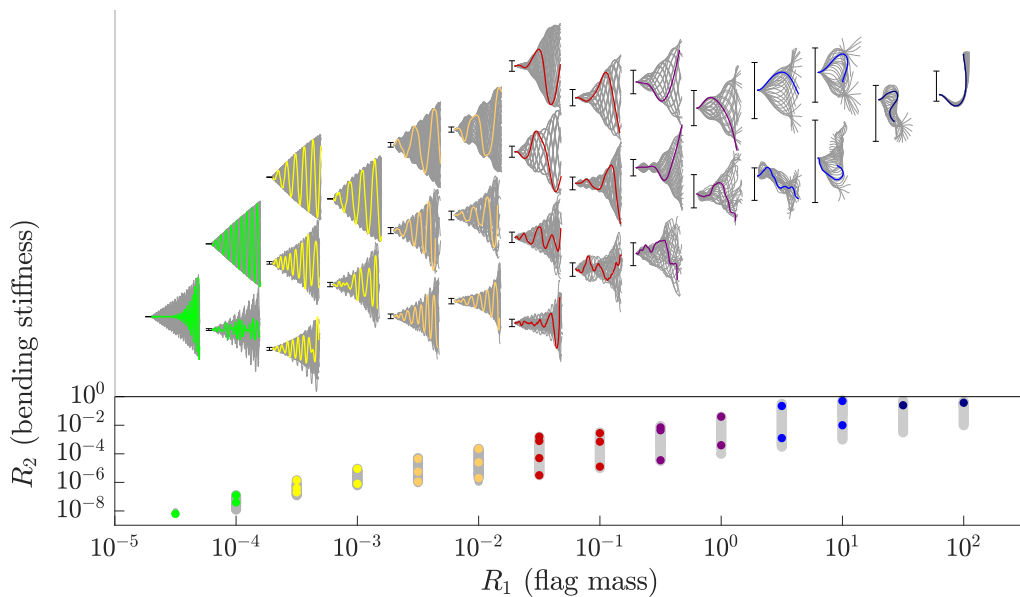


FIG. 2. Sets of flag snapshots at various combinations of flag mass (R_1) and bending stiffness (R_2). Each set of snapshots is scaled vertically to enhance visibility. The true maximum and minimum vertical deflections (relative to the horizontal scales of the flags) are shown by the black scale bars to the left of each set of snapshots. Beneath each of column of flags is a column of dots of the same color, at the corresponding (R_1 , R_2) values.

Behind each colored snapshot is a set of many gray snapshots that indicates the overall flapping motion or envelope. At small R_1 ($\lesssim 10^{-2}$), the envelope width grows almost monotonically from the clamped end, with a profile that changes from linear or concave-down at larger R_2 to concave-up at smaller R_2 . At these smaller R_2 , the envelope width is relatively smooth compared to the individual colored snapshots, which show an irregular series of spatial oscillations of varying amplitude, like wave packets. The vertical deflections are scaled by a constant factor for each set of snapshots, to make them more visible. The true maximum and minimum vertical deflections, relative to the horizontal scales of the flags, are shown by the black scale bars to the left of the clamped leading edges of each flag. The deflection amplitudes become progressively smaller as R_1 decreases, and are barely visible at the smallest R_1 .

At the largest R_1 , the flag undergoes small oscillations about a state with nearly vertical tangent at the trailing edge. Here one would expect that flow separation would also occur on the outside of the curved portion of the flag, violating the assumption that separation is confined to the trailing edge. This may also occur for other cases with $R_1 \gtrsim 10^1$, where the deflections are large and in some cases the tangent is directed upstream at the trailing edge. In general, viscous simulations would be needed to know to what extent the trailing edge separation assumption is violated. In some cases, viscous flag simulations have shown that the boundary layer can remain attached even with very large amplitude flapping and an almost vertical tangent at the trailing edge at certain instants [25], unlike for a static body fixed in a similar configuration.

Having presented examples of typical flag motions, in Fig. 3 we show how three main dynamical quantities vary with R_1 and R_2 in the same region. The values are plotted as colored dots, one per simulation. Figure 3(a) shows the dominant Fourier mode of the vertical deflection, time averaged. We call this quantity the “mode number,” and it is

$$K \equiv \arg \max_{K'} |\hat{Y}_{K'}|, \quad \text{where} \quad y(s) = \sum_{K'=-\infty}^{+\infty} \hat{Y}_{K'} e^{i2\pi K' s}. \quad (11)$$

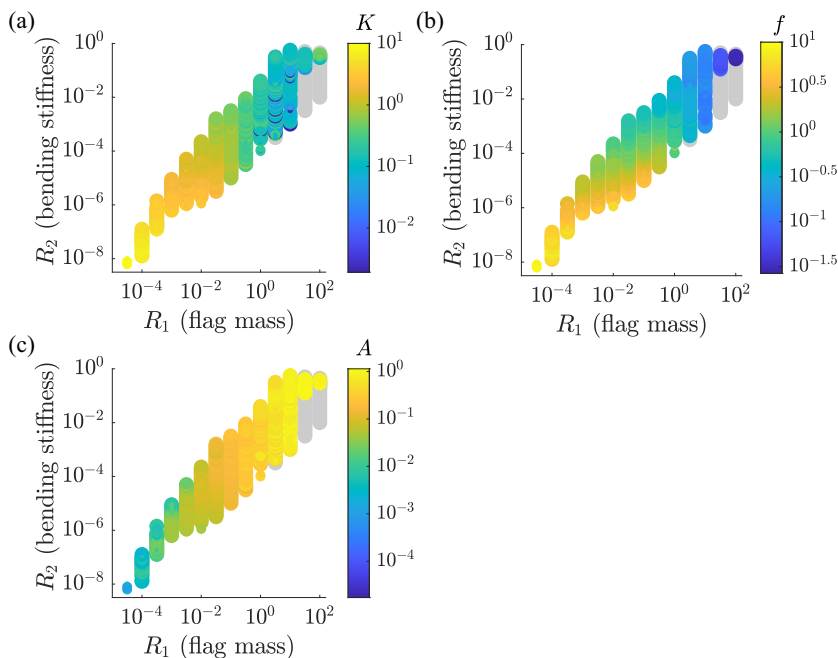


FIG. 3. Measures of flag dynamics across (R_1, R_2) space. (a) Mean mode number, defined by (11), the time average of the dominant Fourier component of the flag deflection. (b) Mean flapping frequency, defined as twice the reciprocal of the time-average duration between sign changes of the free end deflection. (c) Mean flapping amplitude, defined as the root-mean-square deflection of the flag’s free end.

The mode number K can be expressed as a wave number k via $2\pi K = k$. Although the vertical deflection is not a periodic function of s , it has wavelike features in many cases, e.g., in the left half of Fig. 2. We find that the dominant Fourier component of $y(s)$ on the flag has a wavelength close to those of the oscillations on the flag. In Fig. 7 in the Appendix, we compare each flag snapshot in the topmost sets of flag snapshots from the left seven columns in Fig. 2, $10^{-4.5} \leq R_1 \leq 10^{-1.5}$, with the corresponding dominant Fourier modes. The spacings between the peaks of the dominant Fourier modes are seen to closely approximate the spacings for the flags’ deflection oscillations (black, green, yellow, orange, and red in Fig. 7). We also considered using the spacing between deflection peaks as a measure of the flag deflection mode. However, for the motions in Fig. 2 that are somewhat chaotic, there are sometimes closely spaced peaks with just a small decrease in deflection between them. Since the Fourier modes depend on the global shape of the deflection curve, they are less sensitive to slight local perturbations than is the distance between deflection extrema. Figure 3(b) shows the values of mean flapping frequency f . This is the reciprocal of the mean flapping period, which is defined here as twice the mean duration between sign changes of the free end deflection. Figure 3(c) shows the values of the mean flapping amplitude A , defined as the root-mean-square deflection of the free end.

The upper boundary of the colored region in each panel is the stability boundary in $R_1 - R_2$ space. The boundary reaches a plateau for $R_1 \gtrsim 10^1$, and is upward sloping, with a variable slope at smaller R_1 . Here, higher resolution studies have found that the boundary has a scalloped shape [57]. At the largest R_1 , the gray dots mark cases where the initial perturbation grew to a large amplitude, but the flag motion then became very irregular, with stronger deformations than those in Fig. 2. The computations failed to converge at a certain time step before a steady-state large amplitude motion was reached, so steady-state quantities could not be calculated. This tends to occur at large R_1 and small R_2 .

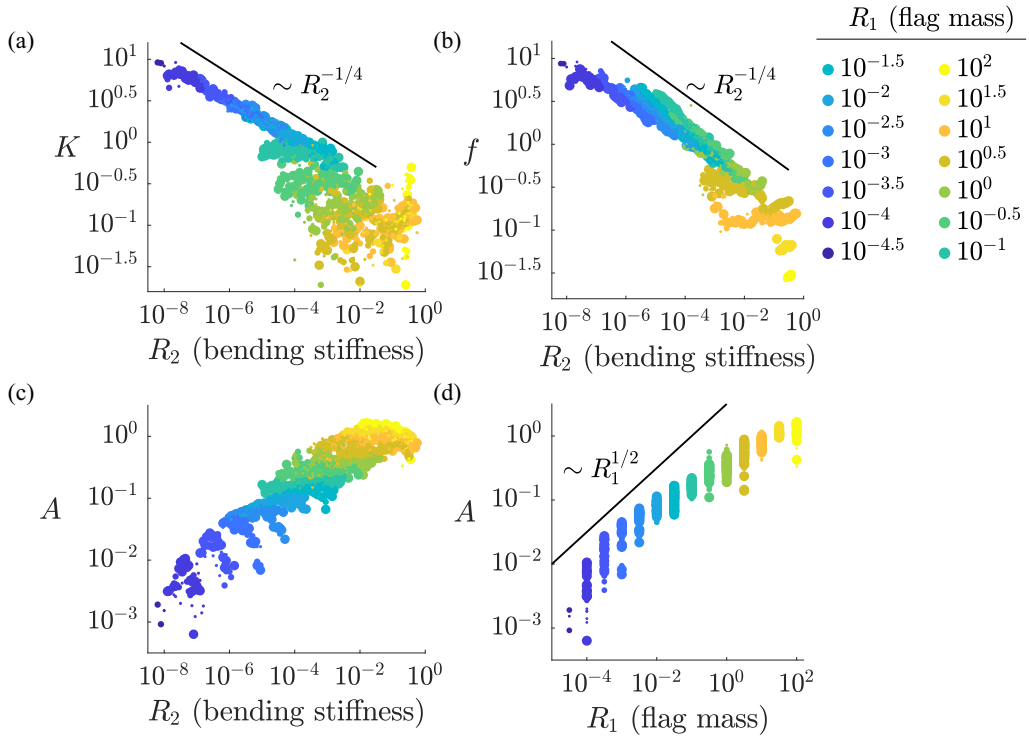


FIG. 4. Power law behaviors of measures of flag dynamics. (a) Mean flag mode number vs R_2 , for various R_1 (labeled by color; see legend at far right). (b) Mean flapping frequency vs R_2 , for various R_1 . (c) Flapping amplitude (root-mean-square vertical displacement at the free end) vs R_2 , for various R_1 . (d) Flapping amplitude vs R_1 , for various R_2 .

Figure 3(a) shows that as R_1 decreases and as R_2 decreases, the mean mode number generally increases to a maximum of about 10 in the lower left portion of this region. On the right side, where the mean mode number is less than 1, there are rapid changes from blue-green to dark-blue dots. Here the deflection pattern does not have a regular series of oscillations (e.g., cases with $R_1 = 10^{0.5}$ and 10^1 in Fig. 2), so at each time the dominant Fourier mode number is either 0 or 1. The time average varies in the range $[0, 1]$ as R_2 decreases and the flag exhibits different types of periodic and chaotic motions. Figure 3(b) shows that the mean frequency has a pattern of nearly monotonic change with R_1 and R_2 , similar to that of the mean mode number. At the largest R_1 , however, the mean frequency continues to decrease, while the mean mode number saturates at an $O(1)$ value. This corresponds to slow flag oscillations in states with large deflections, as shown in the rightmost columns of Fig. 2. Figure 3(c) shows that the root-mean-square (rms) amplitude is $O(1)$ at large R_1 , and progressively decreases to $O(10^{-3})$ as R_1 decreases to $10^{-4.5}$. At a fixed R_1 , and R_2 decreasing from just above the stability boundary value, the amplitude at first jumps to a nonzero value and grows sharply, with a hysteretic transition to flapping [45,58]. The amplitude reaches a maximum and then decreases in a series of complex transitions, as the flag flaps in higher modes and chaotic states [46].

In Fig. 4, we plot the mode number, frequency, and amplitude values from Fig. 3 versus R_2 , with a different color for each R_1 value (shown at right). Figure 4(a) shows that the mean mode number K scales approximately as $R_2^{-1/4}$ for the smaller half of R_1 values, $[10^{-4.5}, 10^{-1.5}]$, ranging from dark blue to light blue. The dots with different R_1 values (different colors) mostly overlap in this range, so the mode number is approximately independent of R_1 . Values are plotted with three

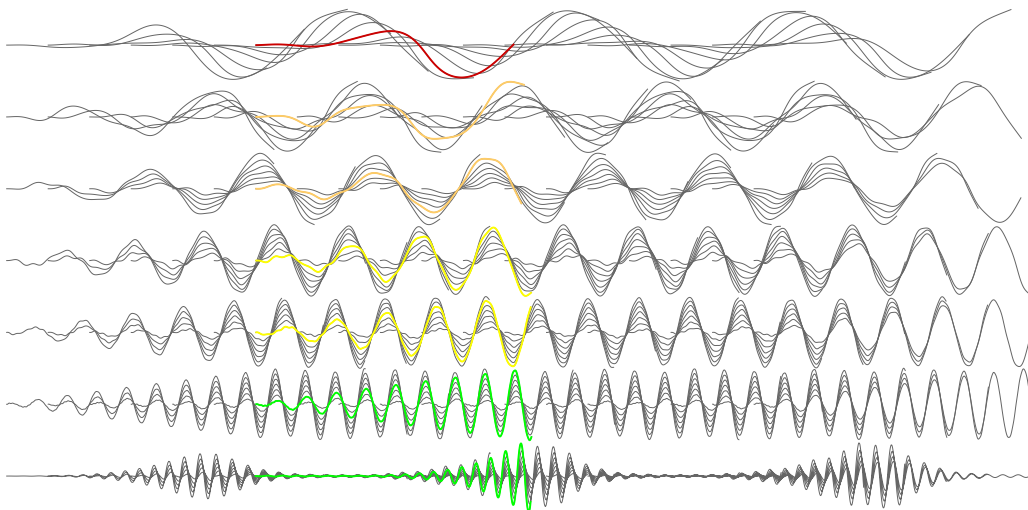


FIG. 5. Flag deflections in the rest frame of the far-field flow. Plotted here are the topmost sets of flag snapshots from the left seven columns in Fig. 2, with $10^{-4.5} \leq R_1 \leq 10^{-1.5}$, with respect to $x - t$ on the horizontal axis (the rest frame of the fluid in the far field). Each set of snapshots is scaled vertically to make the deflections visible.

different numbers of spatial grid points in the simulations, $n = 121, 241,$ and 361 (except at the smallest $R_1 = 10^{-4.5}$, where two n values, 361 and 481 , were used). Although the largest n gives the highest resolution, in some cases the simulations with smaller n ran for longer times, resulting in a larger sample for the time averages. We plot the data for all the n values, with smaller dots for smaller n , to show the degree of variation in these quantities as n varies in this range. At the larger R_1 , i.e., $[10^{-1}, 10^2]$, the mean mode number values spread out to a large degree. This occurs because the values are in the range of 1 or less, so they vary widely on a logarithmic scale but less so in absolute magnitude. The region of K values less than one, i.e., $[10^{-1} \leq R_1 \leq 10^2]$, represents the convergence to states with little or no spatial periodicity.

At small R_1 , Fig. 4(b) shows that the mean frequency agrees well with the mean mode number, not just in the $R_2^{-1/4}$ scaling but also in the magnitudes of the values. This corresponds to motions that are traveling waves with nearly the same speed as the oncoming flow velocity. In Fig. 5, we replot sets of snapshots at the seven smallest R_1 in Fig. 2—those at the top, closest to the stability boundary—with respect to $(x - t)$ in the horizontal direction, i.e., a frame that moves with the far-field flow. The peaks of deflection align if they move at the same speed as the far-field flow. This is approximately the case, more so as we move downward in the figure to smaller R_1 . In general, the peaks move slightly leftward as they increase in this frame, and more so for the higher sets of snapshots, at larger R_1 . Thus, in the original frame, fixed at the flag leading edge, the traveling wave speed is slower than the flow speed, but approaches it as R_1 becomes very small.

Returning to Fig. 4, the mode number [Fig. 4(a)] is approximately constant in R_1 at small R_1 , whereas the frequency [Fig. 4(b)] grows with R_1 , shown by the slight upward shift of the green lines relative to the blue lines. By plotting the data with respect to R_1 (not shown), we find that the growth may be as large as $R_1^{1/4}$ for R_1 in the lower half of logarithmic range studied here. The frequency is approximately constant with respect to R_1 near $R_1 = 10^{-0.5}$, and decays with R_1 at larger R_1 values. Figure 4(c) shows the flapping amplitude plotted with respect to R_2 . The data for a given R_1 (a given color) approximately follow an inverted U-shaped curve, reaching a peak at an R_2 somewhat below the stability boundary and then decreasing, as found in [46]. Figure 4(d) plots the same data with respect to R_1 . The peak amplitudes at each R_1 increase monotonically with R_1 , more rapidly than

$R_1^{1/2}$ at the smallest R_1 , then more slowly at larger R_1 . Figure 8 in the Appendix shows the data in Fig. 4 plotted on separate axes for each R_1 value, without the overlapping of data for different R_1 . These plots show that the $R_2^{-1/4}$ scaling of mode number applies well for $10^{-4} \leq R_1 \leq 10^{-1.5}$, and the same scaling of frequency applies in a somewhat larger range, $10^{-4} \leq R_1 \leq 10^0$.

Next, we discuss scaling law predictions from small-amplitude models, which allow for a quantitative explanation of some of the scaling laws.

IV. SMALL-AMPLITUDE MODEL

Simple analytical results for the flag's large-amplitude motion are difficult to obtain. A simplified model that can be solved analytically is a linearized version of the problem for an infinite periodic flag without a free vortex wake shed from the trailing edge, studied previously in [9,14]. The vortex sheet wake is important, particularly for large-amplitude flapping which creates strong vorticity in the wake. However, the coupled system of a finite flag and trailing wake is difficult to analyze theoretically. Models that neglect the free wake or assume a doubly infinite wake have been used extensively in previous theoretical studies of flapping flags [9,11,27,59,60]. Periodic models were compared with experiments [9,11,39] and with the finite flag model [39,45], and reasonable agreement was found in terms of the location of the stability boundary.

Linearizing Eqs. (1), (5), and (8) about the zero-deflection state, we obtain

$$\partial_t y + \partial_x y = \frac{1}{2\pi} \oint_{-\infty}^{\infty} \frac{\gamma(x', t)}{x - x'} dx', \quad (12)$$

$$\partial_t \gamma + \partial_x \gamma = \partial_x [p], \quad (13)$$

$$R_1 \partial_{tt} y + R_2 \partial_{xxxx} y = -[p]. \quad (14)$$

Solutions to (12)–(14) are given by sinusoidal traveling-wave eigenmodes of the form

$$y(x, t) = \hat{y}_k e^{i(kx + \sigma t)}, \quad \gamma(x, t) = \hat{\gamma}_k e^{i(kx + \sigma t)}, \quad [p](x, t) = [\hat{p}]_k e^{i(kx + \sigma t)}, \quad (15)$$

for each real k . Inserting the modes (15) into (12)–(14), and using the Hilbert transform formula

$$\frac{1}{\pi} \oint_{-\infty}^{\infty} \frac{e^{ikx'}}{x - x'} dx' = -i \operatorname{sgn}(k) e^{ikx}, \quad (16)$$

we obtain the dispersion relation for σ as a function of k ,

$$\sigma = -\frac{2k}{R_1 |k| + 2} \pm \frac{\sqrt{R_1 R_2 k^6 + 2R_2 |k|^5 - 2R_1 |k|^3}}{R_1 |k| + 2}. \quad (17)$$

We have a transition from a neutrally stable pair of modes with real σ to a stable-unstable pair when the quantity under the square root is zero, i.e.,

$$R_2 = \frac{2R_1}{R_1 |k|^3 + 2k^2}, \quad (18)$$

which gives the stability boundary for each k . For a given (R_1, R_2) value, the quantity under the square root in (17) is negative for modes with a certain range of k centered at 0 (i.e., long waves) that are unstable. Within the instability region, where $\sigma = \sigma_R + i\sigma_I$, we now compute k_{\max} , i.e., the value of k that maximizes the growth rate,

$$\sigma_I = \frac{\sqrt{-R_1 R_2 k^6 - 2R_2 |k|^5 + 2R_1 |k|^3}}{R_1 |k| + 2}, \quad (19)$$

and the corresponding $\sigma_{I, k_{\max}}$ and $\sigma_{R, k_{\max}}$ [the first term on the right-hand side of (17)]. Squaring (19) and maximizing it, we find that k_{\max} is a root of a quartic polynomial and can be approximated

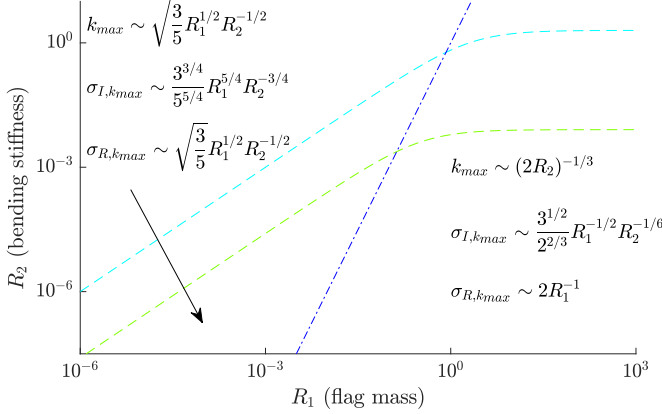


FIG. 6. The two regimes of asymptotic scalings in the instability region for the spatially periodic, small-amplitude model. The blue dash-dotted line $R_1 = R_2^3$ is approximately the location of the transition region between the two regimes. In each regime, the scalings of the fastest growing mode's wave number k_{\max} , corresponding growth rate $\sigma_{I,k_{\max}}$, and angular frequency $\sigma_{R,k_{\max}}$ are listed. The light-blue and light-green lines show examples of stability boundaries that correspond to $k = 2\pi$ (light-green dashed line) and $k = 1$ (light-blue dashed line).

using the method of dominant balance. A formal version of the method leads to the same results as a more informal approach that we state here. We note that there are two different asymptotic regimes, depending on which of the first two terms under the square root in (19)—the stabilizing terms—is dominant—i.e., on whether their ratio $R_1|k|/2$ is small or large. The two terms in the denominator also have this ratio, and thus one or the other is neglected in the same regimes. Neglecting the appropriate terms when $R_1|k|/2$ is small or large, we find

$$R_1|k|/2 \ll 1: \quad k_{\max} \sim \sqrt{\frac{3}{5}} R_1^{1/2} R_2^{-1/2}; \quad \sigma_{I,k_{\max}} \sim \frac{3^{3/4}}{5^{5/4}} R_1^{5/4} R_2^{-3/4}; \quad \sigma_{R,k_{\max}} \sim \sqrt{\frac{3}{5}} R_1^{1/2} R_2^{-1/2}, \quad (20)$$

$$R_1|k|/2 \gg 1: \quad k_{\max} \sim (2R_2)^{-1/3}; \quad \sigma_{I,k_{\max}} \sim \frac{3^{1/2}}{2^{2/3}} R_1^{-1/2} R_2^{-1/6}; \quad \sigma_{R,k_{\max}} \sim 2R_1^{-1}. \quad (21)$$

If we plug the k_{\max} approximations in (20) and (21) into $R_1|k|/2$, we obtain $R_1 R_2^{-1/3} \ll 1$ and $\gg 1$, respectively, in the two regimes. Thus, $R_2 = R_1^3$, plotted as a blue dash-dotted line in Fig. 6, approximately marks the transition between the two regimes.

In Fig. 6, the asymptotic approximations in each regime are listed, and the scalings match in a neighborhood of the blue dash-dotted line. Also plotted are two examples of stability boundaries (18), for two k values of order 1: $k = 1$ (light-blue dashed line) and $k = 2\pi$ (light-green dashed line). For any real k , the stability boundary is linear at small R_1 and horizontal at large R_1 . If we imagine that the finite flag is modeled by the infinite periodic flag with a range of allowed $|k|$ down to a prescribed nonzero minimum value that is comparable to the finite flag length ($k = 2\pi$ corresponds to a half period of a sine function on a flag of length 2, and $k = 1$ a smaller fraction of a period), the stability boundary would have the same form as the dashed lines. These stability boundaries show qualitative agreement with the shape of the stability boundary seen in large-amplitude viscous and inviscid simulations and in experiments [9,39,45]. In these studies, the threshold value of R_2 for instability increases with R_1 at small R_1 and reaches a plateau for $R_1 \gtrsim 1$. Our nonlinear simulation results in Fig. 3 show a stability boundary that is close to the light-blue dashed line for $R_1 \geq 10^{-2}$. For smaller R_1 , the stability boundary in Fig. 3 has a slope that is variable but larger than 1, corresponding to superlinear growth of the critical R_2 with R_1 .

We now compare the scalings of the wave number and frequency of the fastest growing mode in the periodic flag model with the corresponding quantities in the nonlinear simulations. In our previous work on flutter of membranes (with zero bending stiffness) [61,62], we found qualitative similarities in how the membrane frequency and mode shapes vary with membrane mass and stretching stiffness when oscillatory motions occur in both the linear and nonlinear regimes. For the periodic flag, k_{\max} scales as $R_1^{1/2}R_2^{-1/2}$ at small R_1 , and $R_2^{-1/3}$ at large R_1 . For the nonlinear model, we found $k = 2\pi K \sim R_2^{-1/4}$ at small R_1 , and $K \approx 1$ at large R_1 , where the large-amplitude flapping motion is increasingly chaotic and the deflection is not well approximated by a sinusoidal function as R_2 decreases to small values. The angular frequency σ_R becomes equal to the wave number k at small R_1 in the periodic small-amplitude model and the same is true in the large-amplitude model (using $\sigma_R = 2\pi f$ and $k = 2\pi K$), corresponding to traveling waves that move at the speed of the background flow. The waves of deflection are sinusoidal in the periodic model, and sinusoidal with a monotonically growing envelope, from the clamped end to the free end, in the nonlinear model. At large R_1 , the frequency scales as R_1^{-1} in the periodic model. By fixing R_2 and varying R_1 in the large- R_1 regime, a range of decaying behaviors is seen in the nonlinear model, sometimes as rapid as R_1^{-1} . However, the dynamics are not well approximated by sinusoidal traveling waves, and there is a limited range of stable large-amplitude motions for $R_1 > 10^1$. For tethered membranes (with stretching stiffness and zero bending stiffness) at large R_1 , the typical oscillation frequency scales as R_1^{-1} in the linear regime, and changes to $R_1^{-1/2}$ in the nonlinear regime [63]. Here the membranes are stretched between tethers at their ends, so the dynamics are more stable than for the flags with free ends, and the wider range of stable dynamics allows a scaling law to be measured more precisely.

Approximate scaling laws

Having presented linearized solutions in the periodic case, we now consider more approximate arguments, with nonlinear effects but without detailed flow solutions. In the limit of small amplitude, Eloy *et al.* [58] computed a power series expansion in a weakly nonlinear approximation of traveling-wave solutions of the same periodic potential flow model that gives rise to (12)–(14). They found that the leading-order nonlinear term in $[p]$ is $O(|y|^3)$, and is stabilizing, so it would result in a finite-amplitude steady-state solution. Balancing the $O(|y|^3)$ term with $R_1 \partial_{tt}y$ would predict that the deflection amplitude $y \sim R_1^{1/2}$. Because the amplitude is small even for the nonlinear solutions at small R_1 , the weakly nonlinear approximation involving a power series expansion in y is reasonable.

We assume the linearized bending force term $R_2 \partial_{xxxx}y$ in (14) is still the dominant bending force term in the weakly nonlinear case because the nonlinear terms include higher powers of $|y|$, which is small. The term $R_2 \partial_{xxxx}y$ can balance the remaining terms in (14), which are independent of R_2 at leading order, if we assume y varies on a typical x length scale $\sim R_2^{-1/4}$, so $R_2 \partial_{xxxx}y \sim y$. In the weakly nonlinear solution of [58], when $R_1, R_2 \rightarrow 0$ but within the instability region, y is at leading order a traveling wave $Y(x - t)$ that moves at the flow speed (as in the linear growth regime), so the frequency has the same $R_2^{-1/4}$ scaling as the typical wave number.

V. SUMMARY AND DISCUSSION

We have extended the study of large-amplitude (nonlinear) steady-state dynamics of flags to wide ranges of values of flag mass and bending stiffness. This builds on the work of [46], which showed a rich variety of dynamical behaviors as the flow velocity is varied at an intermediate value of flag mass. They found that flapping amplitude and frequency vary over about a factor of 2 as the flow velocity varies over a factor of 20, corresponding to a factor of 400 in the dimensionless bending stiffness parameter that we have used. Here we find a wider range of variation of these quantities and the flag mode number when the flag mass parameter is varied in addition to the bending stiffness. We have shown that the dynamics of flags can be approximated fairly well by power law scalings in

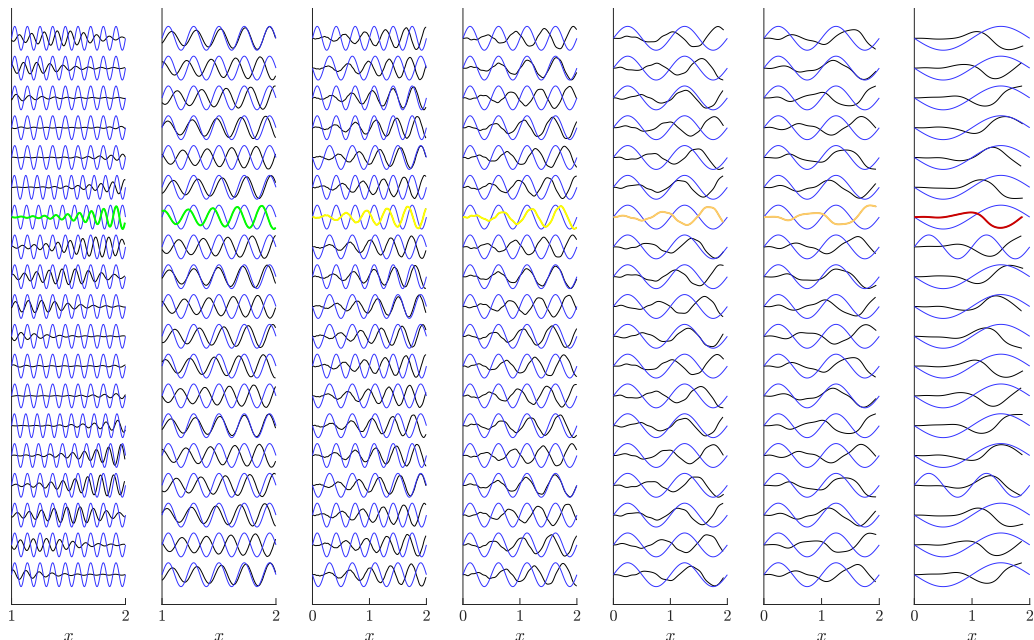


FIG. 7. Comparison between the dominant Fourier modes (blue) and flag snapshots (gray, green, yellow, orange, and red) corresponding to the topmost sets of flag snapshots from the left seven columns in Fig. 2, with $10^{-4.5} \leq R_1 \leq 10^{-1.5}$. These are also the snapshots in Fig. 5. In the left two columns, only the trailing halves of the flags are shown to enhance visibility.

the limit of light, flexible flags. Here the mode number and frequency scale as $R_2^{-1/4}$, corresponding to traveling waves that move at nearly the same speed as the oncoming flow. The flag deflection has many spatial oscillation periods (almost 20 at the smallest R_1 studied, $10^{-4.5}$) and a nearly monotone envelope from the clamped end to the free end. As $R_1 \rightarrow 0$, the flapping amplitude (maximized over R_2) decreases approximately as $R_1^{1/2}$ or faster, reaching values well below 1% of the flag length at the smallest R_1 studied here. We note that very small-amplitude flapping with high wave number and frequency has been previously observed for the inviscid flow model with flags confined to very thin channels, but with much larger values of R_1 [51]. Here, as the channel walls move inward toward the flag, the flag jumps from the unconfined modes shown in the present study to a series of higher bending modes with higher flapping frequencies.

In the linearized periodic model, the solutions are sinusoidal traveling waves, with the unstable region split into two subregions, depending on whether $R_1 R_2^{-1/3}$ is small or large. At small $R_1 R_2^{-1/3}$, the fastest growing modes' wave numbers and frequencies both scale as $R_1^{1/2} R_2^{-1/2}$, corresponding to traveling waves that move at the oncoming flow speed, as in the nonlinear model, but with different power laws. At large $R_1 R_2^{-1/3}$, the wave numbers scale as $R_2^{-1/3}$ and the frequencies as R_1^{-1} . Our nonlinear simulations do not have a traveling-wave character where we have simulation data at large $R_1 R_2^{-1/3}$, but they do show a rapid decay of frequency with R_1 similar to R_1^{-1} . We have considered the effect of a weakly nonlinear stabilizing pressure term and described how an $R_1^{1/2}$ scaling of amplitude, and traveling-wave solutions with $R_2^{-1/4}$ scalings of wave number and frequency, are consistent with this case.

We briefly discuss how some of the quantitative and qualitative relationships we have observed are consistent with physical effects. The strongest effect of the bending stiffness parameter R_2 is to penalize flapping in high-wave-number modes. In the linear growth regime, R_2 decreases the growth rate of high-wave-number modes most strongly. In the large-amplitude regime, larger values of R_2

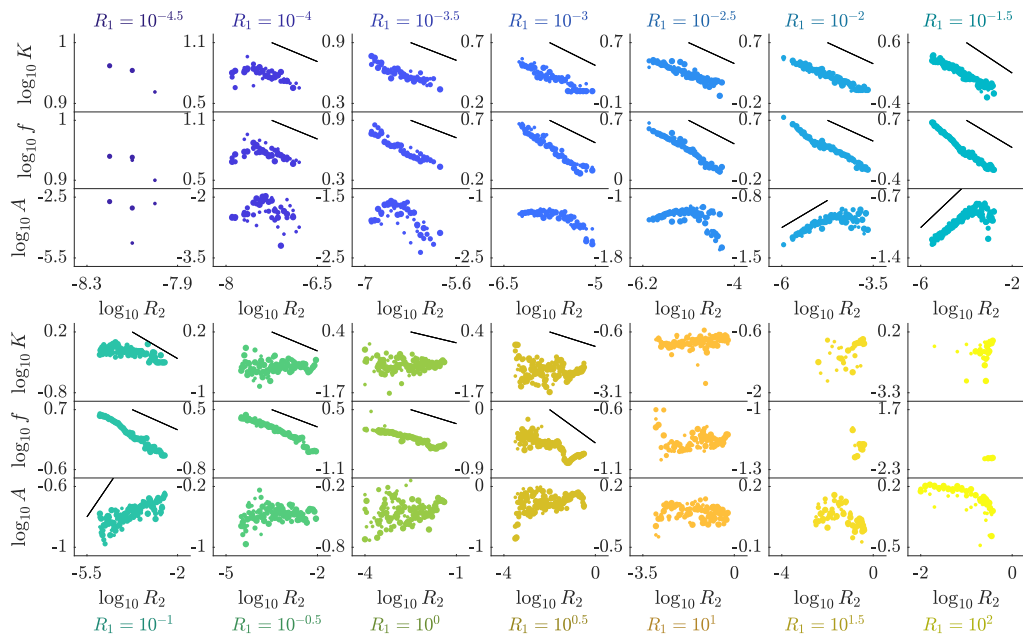


FIG. 8. Plots of mean mode number (K), frequency (f), and amplitude (A) vs R_2 (on horizontal axis). Each column of three subpanels has the same R_1 value (labeled at the top or bottom, in color). In the subpanels for K and f with $10^{-4} \leq R_1 \leq 10^{0.5}$, black lines show the scaling $R_2^{-1/4}$. In the subpanels for A with $10^{-2} \leq R_1 \leq 10^{-1}$, black lines show the scaling $R_2^{1/4}$.

result in a larger bending stiffness force, which can be decreased by flapping in lower-wave-number modes, as occurs in Fig. 4(a). The flag presents a smaller resistance to the flow when it moves as a traveling wave with a speed that is close to that of the oncoming flow, and this is particularly favored at small R_1 and R_2 , where the flag inertia and bending stiffness terms are small and therefore so must be the fluid pressure loading on the flag. Therefore, the ratio of flapping frequency to mode number (or of angular frequency to wave number) is close to the oncoming flow speed (unity), particularly when R_1 and R_2 are small. Flapping amplitude varies nonmonotonically with bending stiffness. The maximum-amplitude value of R_2 may correspond to a resonantlike behavior, as was observed for flexible foils oscillated at the leading edge [64–68].

The clearest effect of the flag mass parameter R_1 is to decrease the flapping frequency at large R_1 , where the flag inertia term strongly resists high-frequency motions. At small R_1 , the flag mass is negligible compared to fluid mass, but is nonetheless essential to the initial instability. The saturated flapping amplitude may grow with R_1 because larger flag inertia allows the flag to maintain its momentum for longer times against fluid resistance, resulting in larger transverse deflections [69,70].

The results we have found are consistent with the previously published flag literature (experimental, computational, and theoretical), comprehensively summarized in [39], in terms of the stability boundary location and the existence of transitions to higher flapping modes as the bending stiffness is decreased. By varying the flag length in an experiment, [71] decreased R_1 and R_2 simultaneously and saw transitions from flapping in a mode with one neck to modes with two, three, and four necks, and then chaotic flapping. Here, R_1 was decreased by a factor of four, remaining close to the $O(1)$ regime. The present paper extends the parameter space to much smaller values of R_1 and R_2 , and it would be interesting to know if these very small-amplitude flapping states, with more than 10 necks in the flapping envelopes (e.g., on the left-hand side of Fig. 2), can be observed experimentally. These occur at very small R_1 , and R_2 close enough to the stability boundary that periodic rather than chaotic flapping occurs.

From a technological point of view, the flags with large mass and moderate stiffness—those that flap with large amplitude—are most likely to be useful for harvesting energy from the flow. The flags with smaller mass and bending stiffness flap with very small amplitudes and seem less useful for energy harvesting. With their weak wakes and small effect on the surrounding flow, they could be more useful as noninvasive flow sensors.

APPENDIX: FLAG DYNAMICS DATA

Figure 7 compares the dominant Fourier mode with the corresponding flag snapshots for the topmost sets of flag snapshots from the left seven columns in Fig. 2, with $10^{-4.5} \leq R_1 \leq 10^{-1.5}$, also the snapshots in Fig. 5.

Figure 8 shows the data from Fig. 4 on separate axes for each R_1 . For K and f , the black lines show the scaling $R_2^{-1/4}$. The scaling applies fairly well for $10^{-4} \leq R_1 \leq 10^{-1.5}$ and, in some cases, with slightly larger R_1 . The amplitude values (A) generally have a maximum at an intermediate R_2 , some distance below the stability boundary. For $10^{-2.5} \leq R_1 \leq 10^{-1}$, a portion of the amplitude data seems to follow a straight line, corresponding to a power law scaling. For reference only, the black line shows the scaling $R_2^{1/4}$ in three panels of A data, though we have no theoretical reason for this scaling.

-
- [1] A. Kornecki, E. H. Dowell, and J. O'Brien, On the aeroelastic instability of two-dimensional panels in uniform incompressible flow, *J. Sound Vib.* **47**, 163 (1976).
 - [2] E. H. Dowell, Nonlinear aeroelasticity, in *New Approaches to Nonlinear Problems in Dynamics*, edited by P. J. Holmes (SIAM Publications, Philadelphia, 1980), pp. 147–172.
 - [3] L. Huang, Flutter of cantilevered plates in axial flow, *J. Fluids Struct.* **9**, 127 (1995).
 - [4] J. Zhang, S. Childress, A. Libchaber, and M. Shelley, Flexible filaments in a flowing soap film as a model for flags in a two dimensional wind, *Nature (London)* **408**, 835 (2000).
 - [5] A. D. Fitt and M. P. Pope, The unsteady motion of two-dimensional flags with bending stiffness, *J. Eng. Math.* **40**, 227 (2001).
 - [6] Y. Watanabe, S. Suzuki, M. Sugihara, and Y. Sueoka, An experimental study of paper flutter, *J. Fluids Struct.* **16**, 529 (2002).
 - [7] L. Zhu and C. S. Peskin, Simulation of a flapping flexible filament in a flowing soap film by the immersed boundary method, *J. Comput. Phys.* **179**, 452 (2002).
 - [8] D. M. Tang, H. Yamamoto, and E. H. Dowell, Flutter and limit cycle oscillations of two-dimensional panels in three-dimensional axial flow, *J. Fluids Struct.* **17**, 225 (2003).
 - [9] M. Shelley, N. Vandenbergh, and J. Zhang, Heavy Flags Undergo Spontaneous Oscillations in Flowing Water, *Phys. Rev. Lett.* **94**, 094302 (2005).
 - [10] M. Argentina and L. Mahadevan, Fluid-flow-induced flutter of a flag, *Proc. Natl. Acad. Sci. USA* **102**, 1829 (2005).
 - [11] C. Eloy, C. Souilliez, and L. Schouveiler, Flutter of a rectangular plate, *J. Fluids Struct.* **23**, 904 (2007).
 - [12] B. S. H. Connell and D. K. P. Yue, Flapping dynamics of a flag in a uniform stream, *J. Fluid Mech.* **581**, 33 (2007).
 - [13] C. Eloy, R. Lagrange, C. Souilliez, and L. Schouveiler, Aeroelastic instability of cantilevered flexible plates in uniform flow, *J. Fluid Mech.* **611**, 97 (2008).
 - [14] S. Alben, The flapping-flag instability as a nonlinear eigenvalue problem, *Phys. Fluids* **20**, 104106 (2008).
 - [15] S. Michelin, S. G. Llewellyn Smith, and B. J. Glover, Vortex shedding model of a flapping flag, *J. Fluid Mech.* **617**, 1 (2008).
 - [16] A. Manela and M. S. Howe, The forced motion of a flag, *J. Fluid Mech.* **635**, 439 (2009).
 - [17] M. J. Shelley and J. Zhang, Flapping and bending bodies interacting with fluid flows, *Annu. Rev. Fluid Mech.* **43**, 449 (2011).

- [18] T. Leclercq, N. Peake, and E. De Langre, Does flutter prevent drag reduction by reconfiguration?, *Proc. R. Soc. A* **474**, 20170678 (2018).
- [19] T. Theodorsen, General theory of aerodynamic instability and the mechanism of flutter, Tech. Rep. No. 496 (NACA, Washington, DC, 1935).
- [20] Y. C. Fung, *An Introduction to the Theory of Aeroelasticity* (Dover, New York, 1955).
- [21] R. L. Bisplinghoff and H. Ashley, *Principles of Aeroelasticity* (Dover, New York, 2002).
- [22] L. Zhu and C. S. Peskin, Interaction of two flapping filaments in a flowing soap film, *Phys. Fluids* **15**, 1954 (2003).
- [23] L. Ristroph and J. Zhang, Anomalous Hydrodynamic Drafting of Interacting Flapping Flags, *Phys. Rev. Lett.* **101**, 194502 (2008).
- [24] S. Alben, Wake-mediated synchronization and drafting in coupled flags, *J. Fluid Mech.* **641**, 489 (2009).
- [25] S. Kim, W.-X. Huang, and H. J. Sung, Constructive and destructive interaction modes between two tandem flexible flags in viscous flow, *J. Fluid Mech.* **661**, 511 (2010).
- [26] J. Lee, D. Kim, and H.-Y. Kim, Contact behavior of a fluttering flag with an adjacent plate, *Phys. Fluids* **33**, 034105 (2021).
- [27] J. Mougél and S. Michelin, Flutter and resonances of a flag near a free surface, *J. Fluids Struct.* **96**, 103046 (2020).
- [28] W.-X. Huang and H. J. Sung, Three-dimensional simulation of a flapping flag in a uniform flow, *J. Fluid Mech.* **653**, 301 (2010).
- [29] F. Tian, X. Lu, and H. Luo, Onset of instability of a flag in uniform flow, *Theor. Appl. Mech. Lett.* **2**, 022005 (2012).
- [30] S. Banerjee, B. S. H. Connell, and D. K. P. Yue, Three-dimensional effects on flag flapping dynamics, *J. Fluid Mech.* **783**, 103 (2015).
- [31] D. Kim, J. Cossé, C. Cerdeira, and M. Gharib, Flapping dynamics of an inverted flag, *J. Fluid Mech.* **736**, R1 (2013).
- [32] A. Goza, T. Colonius, and J. E. Sader, Global modes and nonlinear analysis of inverted-flag flapping, *J. Fluid Mech.* **857**, 312 (2018).
- [33] J. W. Park, J. Ryu, and H. J. Sung, Effects of the shape of an inverted flag on its flapping dynamics, *Phys. Fluids* **31**, 021904 (2019).
- [34] A. Giacomello and M. Porfiri, Underwater energy harvesting from a heavy flag hosting ionic polymer metal composites, *J. Appl. Phys.* **109**, 084903 (2011).
- [35] S. Michelin and O. Doaré, Energy harvesting efficiency of piezoelectric flags in axial flows, *J. Fluid Mech.* **714**, 489 (2013).
- [36] X. Wang, S. Alben, C. Li, and Y. L. Young, Stability and scalability of piezoelectric flags, *Phys. Fluids* **28**, 023601 (2016).
- [37] K. Shoele and R. Mittal, Energy harvesting by flow-induced flutter in a simple model of an inverted piezoelectric flag, *J. Fluid Mech.* **790**, 582 (2016).
- [38] D. M. Tang, D. Levin, and E. H. Dowell, Experimental and theoretical correlations for energy harvesting from a large flapping flag response, *J. Fluids Struct.* **86**, 290 (2019).
- [39] Y. Yu, Y. Liu, and X. Amandolese, A review on fluid-induced flag vibrations, *Appl. Mech. Rev.* **71**, 010801 (2019).
- [40] K. Shoele and R. Mittal, Computational study of flow-induced vibration of a reed in a channel and effect on convective heat transfer, *Phys. Fluids* **26**, 127103 (2014).
- [41] S. G. Park, B. Kim, C. B. Chang, J. Ryu, and H. J. Sung, Enhancement of heat transfer by a self-oscillating inverted flag in a Poiseuille channel flow, *Intl. J. Heat Mass Transf.* **96**, 362 (2016).
- [42] A. Glezer, R. Mittal, and S. Alben, Enhanced forced convection heat transfer using small scale vorticity concentrations effected by flow driven, aeroelastically vibrating reeds, Tech. Rep. No. AFRL-AFOSR-VA-TR-2016-0339 (AFOSR, Arlington, VA, 2016).
- [43] A. Rips, K. Shoele, A. Glezer, and R. Mittal, Efficient electronic cooling via flow-induced vibrations, in *33rd Thermal Measurement, Modeling & Management Symposium (SEMI-THERM), 2017, San Jose, CA, USA* (IEEE, Piscataway, NJ, 2017), pp. 36–39.

- [44] R. K. B. Gallegos and R. N. Sharma, Heat transfer performance of flag vortex generators in rectangular channels, *Intl. J. Therm. Sci.* **137**, 26 (2019).
- [45] S. Alben and M. J. Shelley, Flapping States of a Flag in an Inviscid Fluid: Bistability and the Transition to Chaos, *Phys. Rev. Lett.* **100**, 074301 (2008).
- [46] M. Chen, L.-B. Jia, Y.-F. Wu, X.-Z. Yin, and Y.-B. Ma, Bifurcation and chaos of a flag in an inviscid flow, *J. Fluids Struct.* **45**, 124 (2014).
- [47] S. Alben, Simulating the dynamics of flexible bodies and vortex sheets, *J. Comput. Phys.* **228**, 2587 (2009).
- [48] T. F. H. Runia, K. Gavriluyk, C. G. M. Snoek, and A. W. M. Smeulders, Cloth in the wind: A case study of physical measurement through simulation, in *Proceedings of the IEEE/CVF Conference on Computer Vision and Pattern Recognition, Seattle, WA, 2020* (IEEE, Piscataway, NJ, 2020), pp. 10498–10507.
- [49] W. Bi, P. Jin, H. Nienborg, and B. Xiao, Estimating mechanical properties of cloth from videos using dense motion trajectories: Human psychophysics and machine learning, *J. Vision* **18**, 12 (2018).
- [50] D. House and D. Breen (eds.), *Cloth Modeling and Animation* (AK Peters/CRC Press, Natick, MA, 2000).
- [51] S. Alben, Flag flutter in inviscid channel flow, *Phys. Fluids* **27**, 033603 (2015).
- [52] P. Saffman, *Vortex Dynamics* (Cambridge University Press, Cambridge, 1992).
- [53] R. Krasny, Desingularization of periodic vortex sheet roll-up, *J. Comput. Phys.* **65**, 292 (1986).
- [54] S. Alben, Regularizing a vortex sheet near a separation point, *J. Comput. Phys.* **229**, 5280 (2010).
- [55] T. Y. Hou, J. S. Lowengrub, and M. J. Shelley, Boundary integrals methods for multicomponent fluids and multiphase materials, *J. Comput. Phys.* **169**, 302 (2001).
- [56] S. Alben, The attraction between a flexible filament and a point vortex, *J. Fluid Mech.* **697**, 481 (2012).
- [57] K. Shoele and R. Mittal, Flutter instability of a thin flexible plate in a channel, *J. Fluid Mech.* **786**, 29 (2016).
- [58] C. Eloy, N. Kofman, and L. Schouveiler, The origin of hysteresis in the flag instability, *J. Fluid Mech.* **691**, 583 (2012).
- [59] J. W. Miles, On the aerodynamic instability of thin panels, *J. Aeronaut. Sci.* **23**, 771 (1956).
- [60] C. Q. Guo and M. P. Paidoussis, Stability of rectangular plates with free side-edges in two-dimensional inviscid channel flow, *J. Appl. Mech.* **67**, 171 (2000).
- [61] C. Mavroyiakoumou and S. Alben, Large-amplitude membrane flutter in inviscid flow, *J. Fluid Mech.* **891**, A23 (2020).
- [62] C. Mavroyiakoumou and S. Alben, Eigenmode analysis of membrane stability in inviscid flow, *Phys. Rev. Fluids* **6**, 043901 (2021).
- [63] C. Mavroyiakoumou and S. Alben, Dynamics of tethered membranes in inviscid flow, *J. Fluids Struct.* **107**, 103384 (2021).
- [64] S. Alben, Optimal flexibility of a flapping appendage at high Reynolds number, *J. Fluid Mech.* **614**, 355 (2008).
- [65] S. Michelin and S. G. L. Smith, Resonance and propulsion performance of a heaving flexible wing, *Phys. Fluids* **21**, 071902 (2009).
- [66] H. Masoud and A. Alexeev, Efficient flapping flight using flexible wings oscillating at resonance, in *Natural Locomotion in Fluids and on Surfaces*, edited by S. Childress, A. Hosoi, W. W. Schultz, and J. Wang (Springer, New York, 2012), pp. 235–245.
- [67] F. Paraz, L. Schouveiler, and C. Eloy, Thrust generation by a heaving flexible foil: Resonance, nonlinearities, and optimality, *Phys. Fluids* **28**, 011903 (2016).
- [68] G. A. Tzezana and K. S. Breuer, Thrust, drag and wake structure in flapping compliant membrane wings, *J. Fluid Mech.* **862**, 871 (2019).
- [69] S. Alben and M. Shelley, Coherent locomotion as an attracting state for a free flapping body, *Proc. Natl. Acad. Sci. USA* **102**, 11163 (2005).
- [70] S. Alben, An implicit method for coupled flow-body dynamics, *J. Comput. Phys.* **227**, 4912 (2008).
- [71] E. Virost, X. Amandolese, and P. Hémon, Fluttering flags: An experimental study of fluid forces, *J. Fluids Struct.* **43**, 385 (2013).